Journal of Geochemical Exploration 188 (2018) 326–339

Contents lists available at ScienceDirect

Journal of Geochemical Exploration

journal homepage: www.elsevier.com/locate/gexplo

Evolution of porosity and clay mineralogy associated with chemical weathering of black shale: A case study of Lower Cambrian black shale in Chongqing, China

Sixiang Ling[a,b,*], Xiyong Wu[a,c], Siyuan Zhao[b], Xin Liao[a]

[a] Faculty of Geosciences and Environmental Engineering, Southwest Jiaotong University, Chengdu, Sichuan Province 611756, PR China
[b] Disaster Prevention Research Institute, Kyoto University, Uji, Kyoto 6110011, Japan
[c] Moe Key Laboratory of High-speed Railway Engineering, Ministry of Education, Southwest Jiaotong University, Chengdu, Sichuan Province 610031, PR China

ARTICLE INFO

Keywords:
Black shale
Chemical weathering
Clay mineralogy
Transformation
Pore size distribution
Fractal dimensions

ABSTRACT

This work aimed to evaluate the evolution of pore networks and clay mineral in black shale weathering systems in Chongqing, China. The pore-size distributions, relationships between fractal dimensions and minerals, and clay mineral weathering pathways were evaluated for three weathering profiles, A, B, and C, which were characterized as weak, weak to moderate, and moderate to intense based on the Chemical Index of Alteration. It was found as the shale density decreased, the porosity and specific surface area increased with decreasing depth during weathering. The largest pore diameter peak in a pore-size distribution graph shifted further right as the degree of weathering increased. Micro-transition pores (< 100 nm) dominated the parent shale, while mesopores (0.1–1 μm) and macropores (> 1 μm) dominated the saprock and regolith zones. The surface fractal dimension of the micro-transition pores was positively correlated with the pyrite and carbonate content, but negatively correlated with secondary clay mineral content. By contrast, the surface fractal dimension of the macropores was negatively correlated with pyrite and carbonate content and positively correlated with secondary clay mineral content. These relationships indicate that micro-transition pores at the surface became smoother and macropores became rougher during weathering. Inherited micas, including illite, predominated the clay fractions along transects as weathering proceeded. The pedogenic minerals (i.e., smectite, vermiculite, kaolinite, and mixed-layer minerals) were minor components in the saprock and regolith zones. Smectite formation was likely due to direct transformation from mica or illite under strongly acidic conditions. A second possibility is transformation proceeded through mixed-layer mineral intermediates, i.e., mica-smectite/illite-smectite and mica-vermiculite/illite-vermiculite. The weathering of clay minerals in black shale from weak to intense weathering stages was mica/illite → mica-smectite/illite-smectite or mica-vermiculite/illite-vermiculite → "chlorite" (including vermiculite, hydroxy-interlayered vermiculite?, and chlorite?) → smectite → kaolinite → gibbsite. This study revealed pore geometry evolution depends on transport-limited solutions that facilitate mineral breakdown and formation. The clay mineral weathering pathways were controlled by the weathering environment and duration.

1. Introduction

Chemical weathering is an important rock-altering process that occurs at or near the earth's surface. Weathering increases the water-holding capacity of rock and regolith by increasing porosity and mineral surface area, thereby affecting pore-size and enhancing rates of mineral dissolution and transformation (Cousin et al., 2003; Jin et al., 2011; Perri et al., 2015, 2016). Removal of soluble material and/or elements, such as Ca, Mg, and/or Na, during weathering changes pore structures and surface characteristics, ultimately leading to decreases in solid mass and density and increases in pore diameter and porosity (Fischer and Gaupp, 2005; Jin et al., 2013; Liao et al., 2014; Navarre-Sitchler et al., 2013, 2015). Clay minerals are often a product of weathering, particularly of near-surface supergene conditions. During weathering, pre-existing clay species may transform into other clay phases through a sequence of intermediate interstratified species (Egli et al., 2008a, 2008b; Hong et al., 2012, 2014). In weathering systems, the pore network is the most important physical characteristic of rock because it provides pathways for water flow or infiltration and solute transport. Chemical weathering reactions induce changes in the pore

* Corresponding author at: Disaster Prevention Research Institute, Kyoto University, Uji, Kyoto 611-0011, Japan.
E-mail addresses: lingyou1104@163.com (S. Ling), xinliao@swjtu.edu.cn (X. Liao).

https://doi.org/10.1016/j.gexplo.2018.02.002
Received 8 April 2017; Received in revised form 24 December 2017; Accepted 6 February 2018
Available online 09 February 2018
0375-6742/

network geometry that can alter the rate of fluid transport and, thus, lead to changes in overall rate of mineral weathering (Fletcher et al., 2006; Navarre-Sitchler et al., 2009, 2013).

Black shales contain significant amounts of sulfides and organic matter that can create acidic water under oxidative weathering conditions. Acidic weathering zones for black shale are characterized by intense mineral dissolution and transformation (Jin et al., 2013; Ling et al., 2016). Previous investigations on weathering of black shale and/or sulfide rock have focused predominantly on mineral dissolution, products of sulfide weathering, and mobilization of elements (Jaffe et al., 2002; Fischer et al., 2009; Jin et al., 2010, 2013; Peng et al., 2014; Ling et al., 2015, 2016; Langman et al., 2015; Wu et al., 2015; Wang et al., 2017). Meanwhile, phyllosilicate transformation in black shale weathering zones (Jin et al., 2010; Peng et al., 2014) and of sulfide-bearing rocks (De Kimpe and Miles, 1992; Uzarowicz et al., 2011, 2012), especially in relation to acidic weathering conditions, have received little attention. Previous studies have characterized changes in solute transport that result from alterations in pore diameter and surface characteristics of igneous and metamorphic rock during weathering and rock disaggregation (Chigira et al., 2002; Navarre-Sitchler et al., 2009, 2013, 2015; Jamtveit et al., 2011; Bazilevskaya et al., 2013, 2015; Behrens et al., 2015; Perri et al., 2015, 2016). However, the evolution of pores in black shale during weathering (Fischer and Gaupp, 2005; Jin et al., 2011, 2013) has not been extensively studied. Although previous studies have increased our understanding of pore evolution and phyllosilicate transformation in various rock types (Fischer and Gaupp, 2005; Fischer et al., 2009; Egli et al., 2008a, 2008b; Navarre-Sitchler et al., 2009, 2013; Uzarowicz et al., 2011, 2012; Jin et al., 2010, 2013; Borrelli et al., 2014; Peng et al., 2014), a better understanding of pore evolution and characterization of clay minerals in black shale weathering systems is required. Therefore, this present study aimed to characterize pore evolution and clay mineral transformation pathways in black shale. It is believed the results of this study will increase our knowledge of black shale weathering systems.

Within the black shale weathering systems used in this study, pyrite oxidation was the first weathering reaction to enhance porosity. Subsequently, dissolution of carbonate and plagioclase occurred, increasing pore volume as weathering proceeded (Ling et al., 2016). The origins, formation, and transformation of clay minerals are also important processes during black shale weathering. Pore structure can be significantly affected by both non-clay and clay mineral weathering. To better understand these processes, we investigated pore changes and clay mineral evolution pathways for three different weathering profiles for shale found in the lower Cambrian: (A) mid-ridge, (B) near the mountaintop, and (C) on the valley floor. Profiles A, B, and C were characterized as weak, weak-to-moderate, or moderate-to-intense based on their weathering intensity as evaluated based on the Chemical Index of Alteration (CIA) (Ling et al., 2015, 2016). The objectives of this study were three-fold: (i) to better understand the physical properties of black shale during weathering, (ii) to assess pore size distribution and structure based on fractal dimensions and correlate these with mineral dissolution and/or formation, and (iii) to identify clay fraction evolution and weathering pathways for different weathering stages under acidic weathering conditions.

2. Geological setting

The study area was located in Chengkou County in the northeastern Chongqing Province of China (Fig. 1a), which is situated in the Dabashan tectonic belt. A simplified structural map of Dabashan Mountain is presented in Fig. 1b and a general geological map of the Chengkou area is shown in Fig. 1c. The landscape mainly consisted of low-mountain and valley-landforms covered with broad-leaved trees and bushes. The altitude ranged from 750 to 1250 m and the climate was a subtropical climate zone dominated by East Asian monsoons. The mean annual temperature was 13.8 °C and the average annual rainfall was 1261 mm. The Renhe River flows from southeast to northwest through Chengkou County. Samples were obtained at latitude N31°57′-31°58′ and longitude E108°38′-108°39′ and to the west of the Renhe River. This site was chosen specifically because of excavation activity that provided access to three well-developed vertical profiles (A, B, and C) (Fig. 1d). The three profiles were all from within the Chengba block and were covered by Shuijingtuo Formation black shale. The mineralogy and geochemistry of the three profiles has been previously reported on in detail (Ling et al., 2015, 2016). Variations in the composition of Shuijingtuo Formation shale and its structural complexity make it difficult to distinguish heterogeneity in the three profiles from parent rock. Nevertheless, the bottom sample of every profile was assumed to be parent rock for all three weathering profiles in this present study. Profiles were then subdivided in order into the four zones of parent shale, fractured shale, saprock zone, and regolith zone, where parent rock was deepest and the regolith zone was closest to the surface (Ling et al., 2016).

3. Methods

3.1. Clay mineralogy analysis

Clay fractions (< 2 μm) were separated from bulk shale powder using a previously published sedimentation method (Jackson, 1978; Poppe et al., 2002). Briefly, samples in powder form were dissolved in 20% dilute acetic acid to remove carbonate minerals (Jin et al., 2010) and then treated with 30% H_2O_2 with Calgon to destroy any organic matter. Note these acid and H_2O_2 solutions likely partially dissolve chlorite. The dispersed clay suspensions settled for approximately 60 h. The resulting suspension in the uppermost part of the beaker was then transferred to a polyethylene tube and then centrifuged at 2000 rpm for 5 min to collect the clay fraction. This clay suspension was pipetted onto a glass slide and allowed to dry at room temperature for 48 h. Clay fractions were further treated sequentially by (i) air drying, (ii) Mg-saturation with glycerol (Mg-Glycerol), and (iii) K-saturation and then incubating at 335 °C and 550 °C for 2 h (K-335 °C and K-550 °C, respectively). All treated samples on the glass slides were then analyzed by X-ray diffraction (XRD) using Cu-Kα radiation (PANalytical; Netherlands; 40 kV; 40 mA) from 3° to 30° (15°) 2θ with a counting time of 1 s per 0.02° 2θ step.

3.2. Scanning electron microscopy

For scanning electron microscopy (SEM) analysis, small blocks of individual shale samples were vacuum impregnated and coated with gold. SEM was then performed using a Carl Zeiss Ultra 55 Plus scanning electron microscope (Germany) with an accelerating voltage of 15 kV.

3.3. Density and porosity

Total porosity of the shale samples was roughly estimated based on bulk and particle densities. Briefly, powdered samples were dried at 105 °C overnight and then particle densities (ρ_s) were measured using the pycnometer method and bulk densities (ρ_d) were determined using the paraffin-sealing method (GB/T 50266-2013). Briefly, bulk samples were weighed either without or with paraffin in air and water, respectively. A rough estimate of total porosity (ϕ_t) was calculated as follows:

$$\phi_t = (1 - \rho_d/\rho_s) \times 100\% \quad (1)$$

3.4. High-pressure mercury injection

Samples were crushed and dried in an oven at 105 °C under high vacuum conditions. A Micromeritics AutoPore IV 9500 Porosimeter (USA) was used to record the volume of injected mercury at each

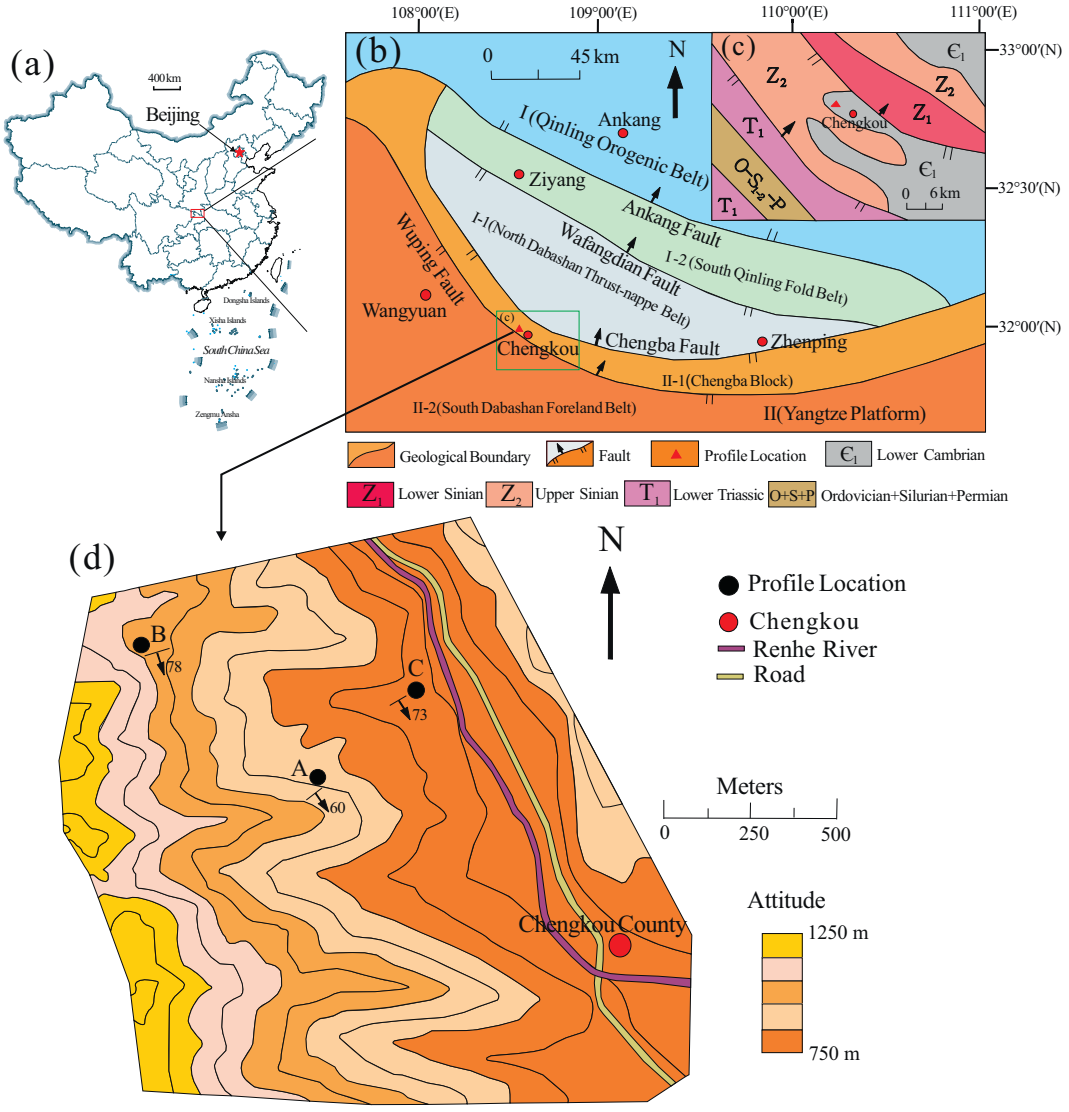

Fig. 1. (a) The general administrative map of China; (b) simplified structural map of Dabashan Mountain; (c) simplified general geological map of Chengkou County from the green box in (b); (d) close-up of study area showing locations of sample profiles in Lower Cambrian black shale in Chengkou County (Ling et al., 2015, 2016); A–mid-ridge; B–near mountaintop; C–valley floor. (For interpretation of the references to colour in this figure legend, the reader is referred to the web version of this article.)

pressure step increase. For the applied pressure, the injection amount at a given pressure is related to pore diameter (d). Assuming cylindrical pores and using the Laplace-Washburn equation (Washburn, 1921),

$$d = \frac{-4\gamma \cos\theta}{P} \times 10^9 \quad (2)$$

where d is pore throat diameter (nm), P is the entry pressure (N/m^2), γ is the interfacial tension (0.485 N/m), and θ is the contact angle (130°).

The pore size distribution of black shale in different zones was included in our high-pressure mercury injection (HPMI) analysis. Results were recorded using Hodot pore-size nomenclature with subdivisions into micropores (< 10 nm), transition-pores (10–100 nm), mesopores (0.1–1 μm), and macropores (> 1 μm). Advection/seepage and diffusion occur predominantly at pore sizes of > 0.1 μm and < 0.1 μm, respectively (Hodot, 1966; Squires and Quake, 2005; Yao et al., 2009; Cai et al., 2013; Fu et al., 2017).

3.5. Low-pressure N_2 gas adsorption

Samples used in low-pressure N_2 gas adsorption (LP-N_2GA) analysis were crushed and sieved through a 60-mesh (< 250 μm). Briefly, low-pressure N_2 adsorption/desorption isotherms were obtained at 77.3 K using a Micromeritics ASAP 2460 (USA) and recording at relative pressures (P/P_0) of 0.01 to 1. The resulting isotherm shapes provided a qualitative assessment of the micro-transition pore shape (2–100 nm) (Kuila and Prasad, 2011). The specific surface area (S_{BET}) was calculated from the N_2 adsorption using the Brunauer-Emmett-Teller method (Brunauer et al., 1938).

3.6. Fractal method

Fractal theory can be used to describe the fractal geometric and structural properties of a solid surface (Pfeifer and Avnir, 1983; Avnir and Farin, 1983). The fractal dimension D is a quantitative index used to characterize the roughness or complexity of a solid surface (Navarre-Sitchler et al., 2013, 2015; Hu et al., 2016; Fu et al., 2017). Two calculation methods based on HPMI and LP-N_2GA have been widely used to characterize pore structure complexity. In this study, the surface fractal dimensions were defined as D_n, D_{m1}, and D_{m2} for micro-transition pores (< 100 nm), mesopores (0.1–1 μm), and macropores (> 1 μm), respectively.

Using the Laplace-Washburn equation (Washburn, 1921), the surface fractal dimension of meso-macropores (> 100 nm) was calculated

Table 1
The physical parameters of black shales in three profiles.

Zonation	Sample	Depth (m)	ρ_d (g/cm^3)	ρ_s (g/cm^3)	ϕ_t (%)	S_{BET} (m^2/g)	± [a] (m^2/g)	pH[b]	*CIA*
Regolith	A-1	0.10	1.53	2.41	36	17.03	0.05	6.03	63.71
	A-2	0.25	1.79	2.45	27	15.58	0.06	4.25	63.30
	A-3	0.45	1.72	2.42	29	13.80	0.02	3.28	63.94
Saprock	A-4	0.55	1.92	2.49	23	10.38	0.04	2.82	63.92
	A-5	0.65	1.90	2.45	23	9.56	0.04	2.68	62.60
	A-6	0.75	1.98	2.49	20	6.08	0.11	3.40	62.60
	A-7	0.85	2.22	2.55	13	3.93	0.08	4.24	56.55
	A-8	1.10	2.42	2.60	7	2.97	0.09	5.88	53.38
Fractured shale	A-9	1.50	2.50	2.64	5	3.91	0.08	6.12	54.25
	A-10	2.10	2.61	2.67	3	2.88	0.08	6.88	54.01
Parent shale	A-11	3.00	2.65	2.69	2	2.14	0.08	6.52	53.65
Regolith	B-1	0.50	1.67	2.48	33	14.87	0.07	7.04	69.12
	B-2	1.00	1.90	2.55	25	7.80	0.05	6.55	66.00
	B-3	1.50	1.88	2.53	25	6.45	0.05	6.62	70.62
Saprock	B-4	2.00	1.75	2.47	29	4.92	0.05	6.20	61.46
	B-5	2.50	1.82	2.54	28	6.70	0.08	6.02	70.82
	B-6	3.20	1.72	2.49	31	6.93	0.06	4.43	65.15
	B-7	4.00	1.98	2.52	21	6.14	0.10	6.50	59.55
Fractured shale	B-8	4.80	2.14	2.53	16	6.67	0.07	6.38	57.98
	B-9	5.50	2.21	2.55	13	5.81	0.06	6.51	57.36
	B-10	6.20	2.38	2.57	7	4.47	0.07	6.80	55.30
Parent shale	B-11	7.00	2.50	2.63	5	3.99	0.10	7.12	52.44
Regolith	C-1	0.50	1.56	2.40	35	14.73	0.07	6.54	79.84
	C-2	1.00	1.49	2.40	38	14.81	0.07	6.40	78.90
	C-3	1.50	1.35	2.41	43	11.03	0.04	6.16	79.09
Saprock	C-4	2.00	1.43	2.40	40	9.60	0.10	6.35	79.42
	C-5	3.00	1.57	2.42	35	10.54	0.07	3.85	79.82
	C-6	4.00	1.79	2.50	28	7.68	0.05	3.70	79.20
	C-7	5.00	1.71	2.48	31	8.72	0.06	4.74	79.62
	C-8	6.20	1.86	2.48	25	7.34	0.17	4.65	79.09
Fractured shale	C-9	8.00	1.90	2.53	25	6.86	0.08	6.83	73.34
	C-10	9.00	2.45	2.58	5	4.22	0.11	7.22	72.97
Parent shale	C-11	10.50	2.74	2.76	1	3.79	0.10	7.26	70.57

ρ_d: bulk density; ρ_s: particle density; ϕ_t: total porosity; S_{BET}: specific surface area, which are computed by BET method from LP-N_2GA data; *CIA*: Chemical Index of Alteration, $CIA = [Al_2O_3 / (Al_2O_3 + CaO^* + Na_2O + K_2O)] \times 100$, and the *CIA* values are derived from Ling et al. (2016).

[a] Standard errors of specific surface area (S_{BET}).

[b] The pH values are derived from Ling et al. (2016).

from HPMI data. This surface fractal dimension is only applicable to meso-macropores because HPMI can damage micro-transition pores (< 100 nm) (Cai et al., 2013). The D_{m1} and D_{m2} were obtained based on thermodynamic principles as follows (Zhang and Li, 1995, Zhang et al., 2006; Mahamud and Novo, 2008):

$$\begin{cases} W_v = \int_0^v PdV \\ D_m = \frac{d\ln(W_v R^{-2})}{d\ln(V^{1/3}R^{-1})} \end{cases} \quad (3)$$

where R is the pore radius (nm) from Eq. (2), V is the cumulative volume (mL/g) of the injected mercury at given pressure P, W_v is the accumulated surface energy (J) in mercury intrusion up to the *n*th stage (Zhang and Li, 1995; Zhang et al., 2006), P is the absolute injection pressure (MPa), and D_m is the surface fractal dimension. The D_m equals the slope of $\ln(W_v R^{-2})$ versus $\ln(V^{1/3}R^{-1})$.

The D_n can be determined from N_2 adsorption data using the Frenkel-Halsey-Hill model. This model can be used for adsorbent-adsorbate interactions in multilayers (Pfeifer and Avnir, 1983) and can be described as follows (Ahmad and Mustafa, 2006; Tang et al., 2015; Hu et al., 2016; Fu et al., 2017):

$$\ln(V) = C + A\left[\ln\left(\ln\left(\frac{P_0}{P}\right)\right)\right] \quad (4)$$

where V is the volume (cm^3/L) of adsorbed gas at equilibrium pressure P, P_0 represents the gas saturation pressure (MPa), P represents the equilibrium pressure (MPa), C is a constant, and A_1 represents the slope of the double logarithm curve of lnV versus $\ln(\ln(P_0/P))$. In general, the D_n for pores < 100 nm can be calculated using $D_n = A + 3$ (Tang et al., 2015; Hu et al., 2016).

4. Results

4.1. Density, porosity, and S_{BET}

The bulk and particle density of black shale are presented in Table 1. Black shale bulk density decreased the closer the sample was to the surface, regardless of sampling site location. These densities ranged from 2.65 to 1.53 g/cm^3, 2.50 to 1.67 g/cm^3, and 2.74 to 1.35 g/cm^3 in profiles A, B, and C, respectively. Very low bulk densities were observed at the surface for profiles A and B and at the bottom of the regolith zone of profile C. Particle densities also decreased moving towards the surface and ranged from 2.69 to 2.41 g/cm^3, 2.63 to 2.47 g/cm^3, and 2.76 to 2.40 g/cm^3 in profiles A, B, and C, respectively. The particle density sharply decreased at the top of the transect due to the addition of organic matter on the surface of the mineral grain. Reductions in bulk density were larger than for particle density.

The total porosities, which were calculated using Eq. (1), increased from 2, 5, and 1% near the parent shale to 36, 33, and 43% in the regolith zones of profiles A, B, and C, respectively. The S_{BET} calculated from the N_2 adsorption isotherms using the Brunauer-Emmett-Teller method are presented in Table 1. The S_{BET}s ranged from 2.14 to 17.03, 3.99 to 14.87, and 3.79 to 14.81 m^2/g for profiles A, B, and C, respectively. The S_{BET} increased as the degree of weathering increased, which is consistent with the decreases in the bulk and particle densities and increases in porosity.

Table 2
Mineral compositions of clay fractions (< 2 μm) and relative proportions of minerals identified in three profiles based on XRD analysis.

Zonation	Sample	Depth (m)	M/I	I-S/M-S	I-V/M-V	V	HIV	Ch	S	K	G
Regolith	A-1	0.10	+ + + +	+ +	−	−	−	−	?	+	−
	A-2	0.25	+ + + +	+	−	−	−	−	+	+ +	−
	A-3	0.45	+ + + +	+	−	−	−	−	+ +	+ +	−
Saprock	A-4	0.55	+ + + +	+	−	−	−	−	+	−	−
	A-5	0.65	+ + + +	+	−	−	−	−	+	−	−
	A-6	0.75	+ + + +	−	−	−	−	−	−	−	−
	A-7	0.85	+ + + +	−	−	−	−	−	−	−	−
	A-8	1.10	+ + + +	−	−	−	−	−	−	−	−
Fractured shale	A-9	1.50	+ + + +	−	−	−	−	−	−	−	−
	A-10	2.10	+ + + +	−	−	−	−	−	−	−	−
Parent shale	A-11	3.00	+ + + +	−	−	−	−	−	−	−	−
Regolith	B-1	0.50	+ + + +	+ (?)	+ +	−	−	+ (?)	+	+ +	−
	B-2	1.00	+ + + +	?	+	−	+	+	+	+	−
	B-3	1.50	+ + + +	+	+	−	+	+	+ +	+	−
Saprock	B-4	2.00	+ + + +	+	−	−	−	−	+	+	−
	B-5	2.50	+ + + +	+	−	−	−	−	+	+	−
	B-6	3.20	+ + + +	?	−	−	−	−	+	−	−
	B-7	4.00	+ + + +	?	−	−	−	−	−	−	−
Fractured shale	B-8	4.80	+ + + +	−	−	−	−	−	−	−	−
	B-9	5.50	+ + + +	−	−	−	−	−	−	−	−
	B-10	6.20	+ + + +	−	−	−	−	−	−	−	−
Parent shale	B-11	7.00	+ + + +	−	−	−	−	−	−	−	−
Regolith	C-1	0.50	+ + + +	+ (?)	+ (?)	+	+ +	−	+	+ +	+
	C-2	1.00	+ + + +	+	+	+	+ +	−	+	+ +	?
	C-3	1.50	+ + + +	+ (?)	+ (?)	+	+ +	−	+ +	+ +	−
Saprock	C-4	2.00	+ + + +	+	?	+	−	−	+	+ +	−
	C-5	3.00	+ + + +	?	?	+	−	−	+	+	−
	C-6	4.00	+ + + +	+	−	−	−	−	−	−	−
	C-7	5.00	+ + + +	+	−	−	−	−	−	−	−
	C-8	6.20	+ + + +	?	−	−	−	−	−	−	−
Fractured shale	C-9	8.00	+ + + +	−	−	−	−	−	−	−	−
	C-10	9.00	+ + + +	−	−	−	−	−	−	−	−
Parent shale	C-11	10.50	+ + + +	−	−	−	−	−	−	−	−

M: mica; I: illite; I-S: illite-smectite mixture phase; M-S: mica-smectite mixture phase; I-V: illite-vermiculite mixture phase; M-V: mica-vermiculite; V: vermiculite; Ch: chlorite; HIV: hydroxy-interlayered vermiculite; G: gibbsite; S: smectite; K: kaolinite.
−: not identified; ?: uncertain occurrence; + (?): uncertain in minor amounts; +: present in minor amounts; + +: present in moderate amounts; + + + +: present in very large amounts.

4.2. Clay fraction mineral composition

4.2.1. Clay mineral identification

Results of clay fraction (< 2 μm) XRD analysis of the three profiles are summarized in Table 2 and representative XRD patterns are shown in Figs. 2–4. Mica, which included illite, was identified under all conditions based on the presence of basal reflections 001, 002, and 003 at 1.0, 0.5, and 0.333 nm (quartz was not considered here), respectively, which did not change position after diagnostic tests (Poppe et al., 2002).

Smectite was identified in air-dried clay-fraction samples at 1.2 and 1.5 nm, where a shift to approximately 1.8 nm was observed after Mg-Glycerol treatment.

Kaolinite was identified in air-dried samples based on the presence of basal reflections at 0.715 and 0.358 nm. These reflections did not shift significantly after treatment with either Mg-Glycerol or K-saturation with heating to 335 °C, but disappeared upon heating to 550 °C.

Vermiculite was identified in the air-dried samples based on the basal 001 reflection at 1.4 nm. The same basal 001 reflection was present at 1.4 nm after Mg-Glycerol treatment. By contrast, the 001 reflection moved to 1.0 nm and formed an asymmetric peak after K-saturation and heating to both 350 and 550 °C. Hydroxy-interlayered vermiculite (HIV) manifested in the incomplete collapse of the basal 001 reflection into a broad peak after K-saturation and heating to 335 °C. Meanwhile, this 1.4 nm peak disappeared and shifted to 1.0 nm after heating to 550 °C.

Chlorite (Ch) was identified based on the basal 001 reflection near 1.4 nm, which did not change position after Mg-Glycerol or K-saturation treatment, even persisting following K-saturation with heating to 550 °C. However, chlorite was dissolved upon using a 2 mol/L HCl solution (Jackson, 1978). The chlorite structure was partly affected by the clay treatment, resulting in a decrease in the intensity or disappearance of the chlorite XRD peak.

4.2.2. Profile A, mid-ridge

Results from the XRD analysis and representative clay sample patterns from profile A are shown in Table 2 and Fig. 2. Characteristic clay phase reflections below 0.85 m (A-7 to A-11) were at 1.0, 0.7, and 0.333 nm, indicating that mica (muscovite in this study) and illite were preserved in parent and fractured shale, as well as deeper portions of the saprock zone. At the upper parts of the saprock zone, smectite was identified in air-dried samples based on the presence of a reflection at 1.28 nm that shifted to approximately 1.8 nm after Mg-Glycerol treatment (Poppe et al., 2002; Skiba, 2007; Uzarowicz et al., 2011).

In the regolith zone, mica (including illite) dominated the clay fraction (Table 2). Kaolinite was identified in the regolith zone based on 0.715 and 0.358 nm reflections in air-dried samples, Mg-Glycerol-treated samples, and K-335 °C-treated samples, and the disappearance of the 0.715 nm reflection in K-550 °C-treated samples (Fig. 2). Mixed-layer clays containing swelling interlayers, most likely illite-smectite (I-S) or mica-smectite (M-S), developed in the regolith zone and were identified based on reflections at 1.1–1.2 nm in air-dried samples that shifted to 1.2–1.4 nm after Mg-Glycerol treatment. These mixed-layer mineral composites increased with weathering, as indicated by the increasing reflection intensity. The reflected peaks of mixed-layer minerals (I-S/M-S) that had been air-dried and treated with Mg-Glycerol also shifted to lower angles as sample location moved closer to the surface (A-3 → A-1).

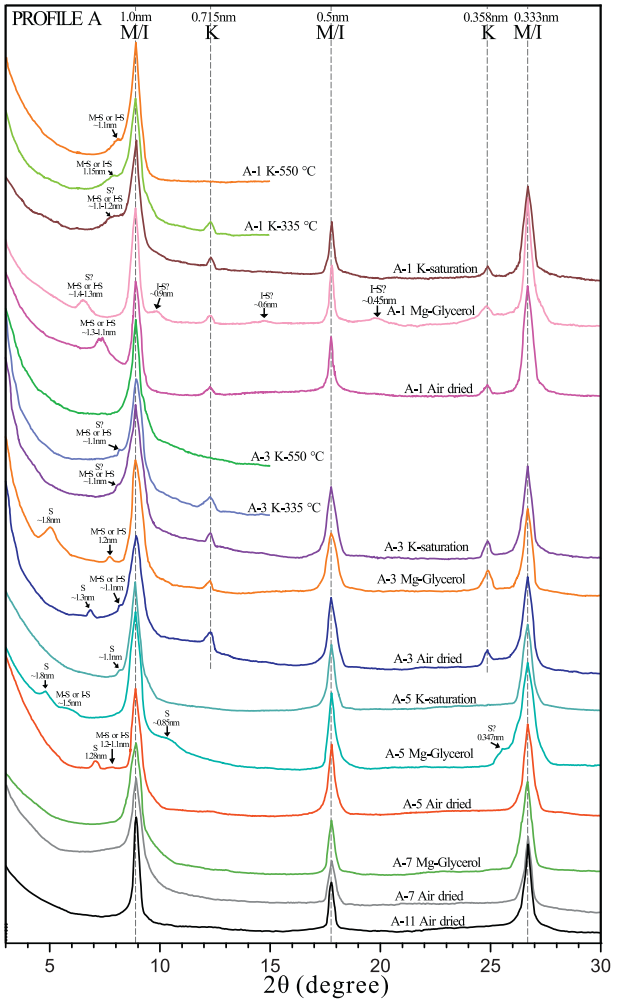

Fig. 2. The XRD patterns of representative samples showing the clay composition in profile A (interplanar spacing unit in nm). Mg-Glycerol: Mg-saturated with glycerol-solvated; K-saturation: K-saturated in air condition; K-335 °C: K-saturated with heated to 335 °C; K-550 °C: K-saturated with heated to 550 °C. Mineral symbols for Figs. 2–4 and text, I: illite, M: mica (muscovite), S: smectite, K: kaolinite, V: vermiculite, Ch: chlorite, G: gibbsite; HIV: hydroxy-interlayered vermiculite, M-S: mica-smectite; M-V: mica-vermiculite, I-S: illite-smectite, I-V: illite-vermiculite.

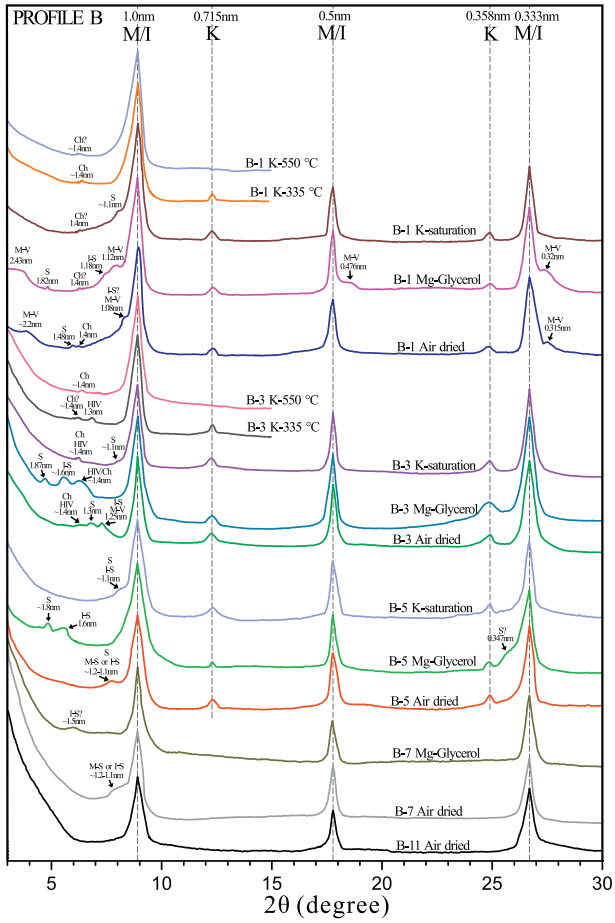

Fig. 3. The XRD patterns of representative samples showing the clay composition in profile B (interplanar spacing unit in nm). Mineral symbols are the same as for Fig. 2.

4.2.3. Profile B, near the mountaintop

XRD results and representative clay fraction patterns for profile B are shown in Table 2 and Fig. 3. Mica (including illite) was present across the entire profile with 1.0, 0.7, and 0.333 nm reflections that did not shift under any treatment conditions. Mica (including illite) was preserved in the parent and fractured shale zones. From the bottom (B-7) to the top of the saprock zone (B-4), M-S or I-S likely formed, as indicated by the formation of a weak peak at 1.1–1.2 nm in air-dried samples that shifted to approximately 1.5–1.6 nm after Mg-Glycerol treatment. Clay fractions in the upper saprock zone were dominated by smectite and kaolinite.

A mica-vermiculite (M-V) mixed-layer was identified in the regolith samples based on the appearance of a reflection between 1.0 and 1.4 nm after Mg-Glycerol treatment. However, this reflection disappeared after K-saturation and heating to 350 and 550 °C. HIV was identified in the regolith zone based on the reflection at 1.4 nm after air dried, Mg-Glycerol, and K-saturated treatment, while the 1.4 nm reflection shifted to 1.3 nm in K-335 °C-treated samples and then shifted to 1.0 nm in K-550 °C-treated samples. This suggests the presence of HIV in the regolith samples. Chlorite was identified in the regolith samples based on a reflection at 1.4 nm that did not shift after any diagnostic treatments. The XRD pattern for sample B-1 after Mg-Glycerol treatment included a superstructure reflection at 2.43 nm. This reflection disappeared after K-saturation and heating to either 335 or 550 °C treatment, indicating that the presence of a small amount of M-V. Smectite, I-S, and kaolinite were also identified in the regolith zone.

4.2.4. Profile C, valley floor

According to XRD analysis and patterns obtained for profile C (Table 2 and Fig. 4), the clay phases in the parent and fractured shales (C-11 to C-8) had characteristic reflections at 1.0, 0.7, and 0.333 nm, suggesting a composition of primarily mica (including illite). Smectite was identified in the air-dried samples at 1.2–1.5 nm in the upper portion of the saprock zone to the regolith zone (C-5 to C-1). This expanded to approximately 1.8 nm after Mg-Glycerol treatment. M-S and I—S were present in both the saprock and regolith samples (C-8 to C-1) as identified in air-dried samples as reflections at 1.1–1.2 nm that shifted to 1.2–1.4 nm after Mg-Glycerol treatment.

The increase in intensity for the 1.4 nm reflection of air-dried samples following Mg-Glycerol treatment suggests vermiculite was present in the samples. Moreover, the intensity of the 1.4 nm reflection decreased after K-saturation and heating to either 335 and 550 °C. Collectively, these results suggest that vermiculite was present in the upper saprock and regolith zones (C-5 to C-1). When K-saturated samples from the regolith zone were heated to 335 °C, the 1.4 nm reflection shifted to 1.36 nm/1.25 nm and the intensity of the 1.0 nm reflection increased. This suggests the presence of HIV in the C-3 to C-1 samples. Meanwhile, 1.36 nm /1.25 nm reflections shifted to 1.0 nm when samples were heated to 550 °C, indicating that the 1.4 nm reflection resulted from HIV in the regolith materials (Harris et al., 1992). Clay-fraction XRD patterns of samples from the upper portion of the

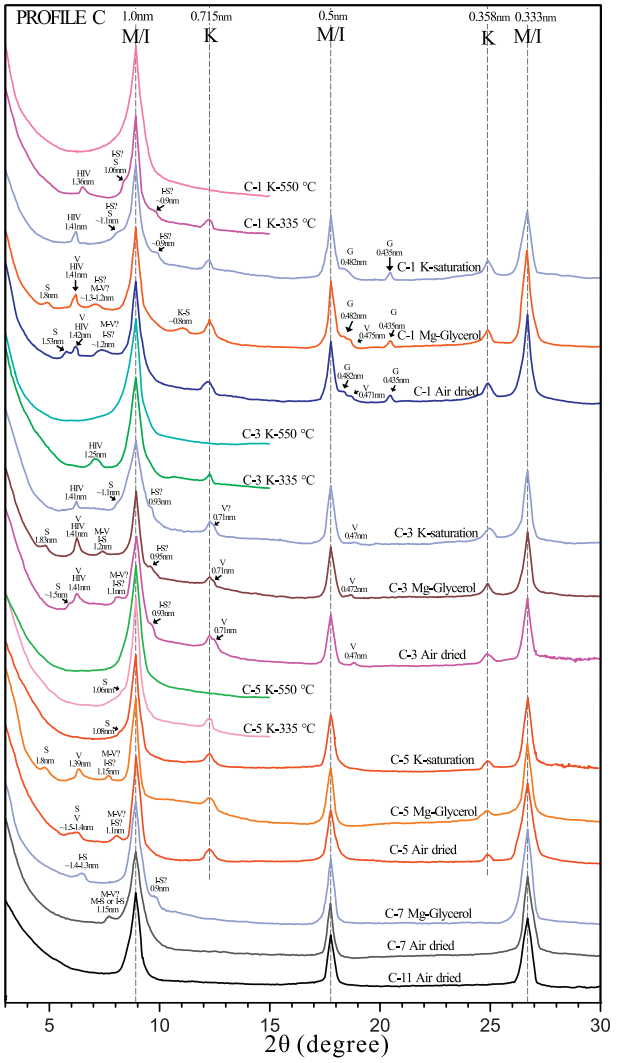

Fig. 4. The XRD patterns of representative oriented clay samples in profile C (interplanar spacing unit in nm). Mineral symbols are the same as for Fig. 2.

saprock zone to the regolith zone (C-5 to C-1) included a broad peak between 1.0 nm and 1.4 nm after Mg-Glycerol treatment that disappeared after K-saturation, indicating the existence of a mixed-layer of M-V.

In the C-1 sample, the peak observed at 0.715 nm shifted to approximately 0.8 nm after Mg-Glycerol treatment, which may be a result of kaolinite-smectite (K-S) interstratification (Schultz et al., 1971; Dudek et al., 2007; Hong et al., 2012). Gibbsite was present in C-1 air-dried samples and was identified based on reflections at 0.482 and 0.435 nm that were unaltered by Mg-Glycerol treatment. Taken together, these results indicate the presence of a K-S mixed-layer and gibbsite minerals at the top of the regolith zone.

4.3. Pore size distribution as determined by HPMI

Pore volumes and percentages for shales in different zones are summarized in Table 3. Total pore volumes ranged from 0.0055 to 0.2379 mL/g, 0.0195 to 0.1944 mL/g, and 0.0024 to 0.3189 mL/g in profiles A, B, and C, respectively. Based on pore percentages, parent shale was primarily composed of micro-transition pores (≥61%), as well as 36 and 28% macropores in profiles A and B, respectively. The dV/dlog(d) versus d (pore diameter) plot calculated from the differential pore volume curve was identical to the pore size distribution and reflected the concentrations of pore sizes (Yao et al., 2009; Hu et al., 2016). The plots of dV/dlog(d) versus d for the three profiles are presented in Fig. 5. Based on the resulting peak patterns, these plots were categorized as unimodal, bimodal, and multimodal (Hu et al., 2016).

Table 3
Total pore volume and pores percentage at different diameters of shales from HPMI.

Zonation	Sample	Depth	V_{total}[a]	Micro-transition pore[b]	Mesopore[b]	Macropore[b]
		(m)	(mL/g)	(%)	(%)	(%)
Regolith	A-1	0.10	0.2379	20	18	62
	A-2	0.25	0.1498	22	15	62
	A-3	0.45	0.1667	24	22	55
Saprock	A-4	0.55	0.1192	23	32	45
	A-5	0.65	0.1180	21	52	26
	A-6	0.75	0.1030	18	57	25
	A-7	0.85	0.0563	31	40	29
	A-8	1.10	0.0283	50	21	29
Fractured shale	A-9	1.50	0.0207	44	15	41
	A-10	2.10	0.0086	61	4	35
Parent shale	A-11	3.00	0.0055	63	1	36
Regolith	B-1	0.50	0.1944	14	41	45
	B-2	1.00	0.1339	16	45	39
	B-3	1.50	0.1309	10	38	52
Saprock	B-4	2.00	0.1662	9	41	50
	B-5	2.50	0.1530	15	42	43
	B-6	3.20	0.1784	16	39	45
	B-7	4.00	0.1077	21	41	38
Fractured shale	B-8	4.80	0.0734	32	48	20
	B-9	5.50	0.0600	30	54	16
	B-10	6.20	0.0305	47	30	23
Parent shale	B-11	7.00	0.0195	61	11	28
Regolith	C-1	0.50	0.2243	14	18	68
	C-2	1.00	0.2508	14	16	70
	C-3	1.50	0.3189	15	14	71
Saprock	C-4	2.00	0.2821	21	13	65
	C-5	3.00	0.2235	22	17	61
	C-6	4.00	0.1585	21	16	63
	C-7	5.00	0.1772	25	17	58
	C-8	6.20	0.1367	21	31	48
Fractured shale	C-9	8.00	0.1311	28	20	52
	C-10	9.00	0.0221	23	34	43
Parent shale	C-11	10.50	0.0024	85	9	6

[a] V_{total} represents total pore volume from HPMI data.
[b] Micro-transition pores: < 100 nm; mesopores: 0.1–1 μm; macropores: > 1 μm.

In profile A, the parent shale (A-11) had the lowest volume of pores with a unimodal peak for transition-pores positioned at approximately 17 nm. In the fractured shales (Fig. 5a), the tallest peak was from micro-transition pores. Samples from the saprock zone (Fig. 5b) plotted as either bimodal or multimodal with the tallest peak being for the primary pore type, mesopore, which is consistent with our results regarding mesopore percentage (21–57%). Transition-pore peaks were observed at 30–40 nm for all saprock materials with peak values approximately 2- to 4-fold greater than in fractured and parent shales. In the regolith zone (Fig. 5c), all samples had bimodal plots. The tallest peak shifted from the mesopore position (~0.8 μm) towards the bottom of the regolith zone to the macropore positon (~6 μm) at the surface. The dominant pores in the regolith zone were macropores (55–62%). The second plot peaks at the transition-pore position for the regolith zone were larger than those obtained from saprock samples.

In profile B, the parent shale displayed a multimodal plot, where three peaks were observed corresponding to the micropore (~8 nm), transition-pore (~30 nm), and macropore (~9 μm) positions. The micro-transition pores were the dominant form in the parent rock, making up 61% of pores (Fig. 5d, Table 3). The fractured shale had a bimodal plot, where the peaks were tallest for the transition-pore region (~30 nm) in sample B-10 and mesopore region (0.1–0.2 μm) in the

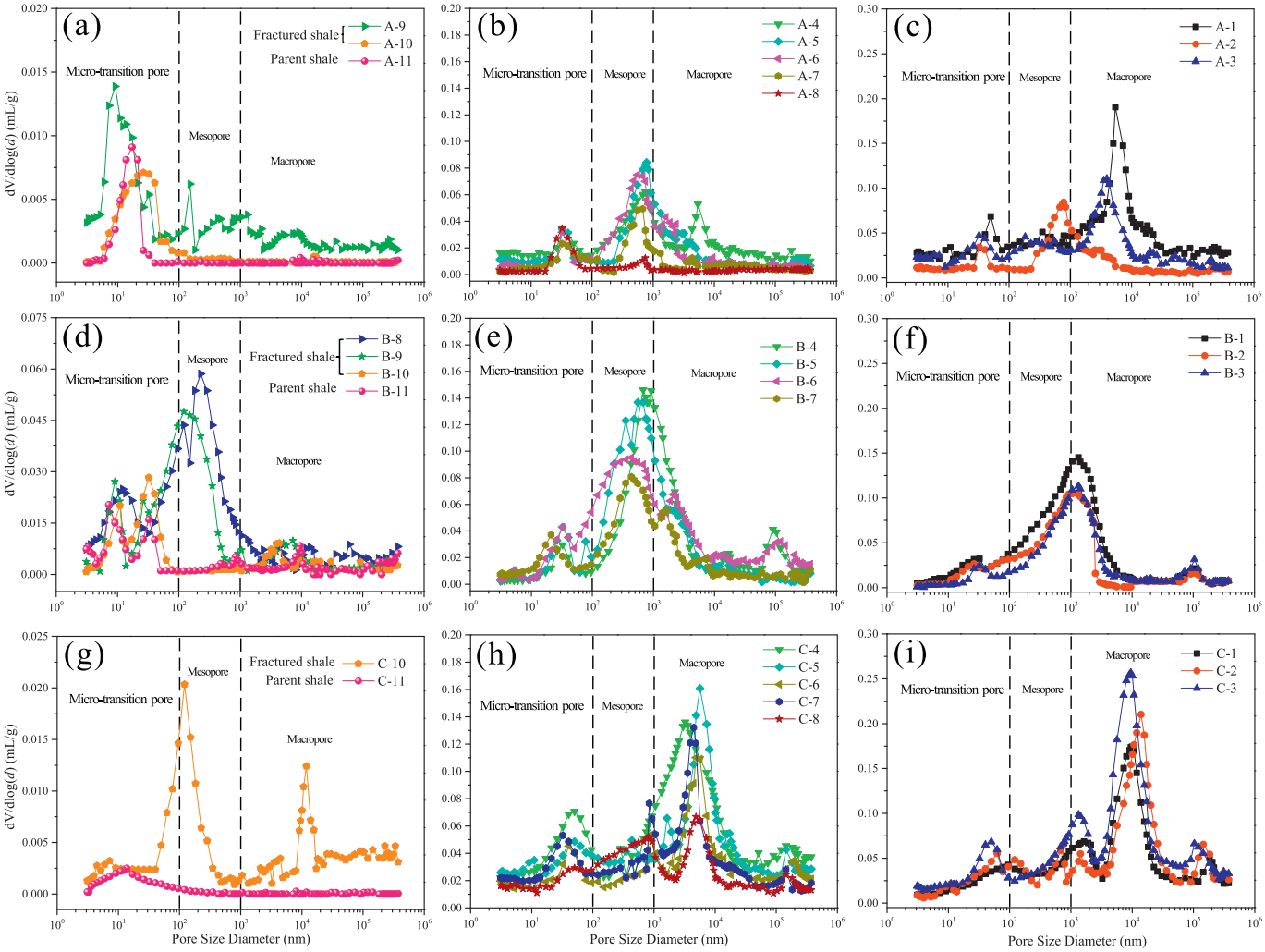

Fig. 5. Pore size diameters of black shales in different zones from high-pressure mercury injection (HPMI). (a–c) profile A; (d–f) profile B; (g–i) profile C. Parent and fractured shale zone in (a), (d), and (e); Saprock zone in (b), (e), and (h); Regolith zone in (c), (f), and (i).

upper parts of the fractured shale zone. In the saprock zone (Fig. 5e), samples had multimodal plots for pore size distribution. These distributions were concentrated in the mesopore range, where the tallest pore peak was located at 0.5–0.9 μm and the pores were primarily 0.1 to 10 μm in size. The transition-pore peak shifted from approximately 10 nm in the fractured and parent materials to 20–40 nm in the saprock zone, indicating the transition-pore diameters increased as weathering proceeded. Macropore dwarf peaks appeared primarily at 1–3, 5–8, and 80–200 μm in saprock materials. In the regolith zone (Fig. 5f), pore plots were multimodal with the tallest peaks positioned at 1–2 μm. The pore sizes were primarily 0.1–3 μm meso-macropores. In addition, the tallest pore peak shifted right as the depth decreased from the transition-pore to the macropore position (Fig. 5d–f).

In profile C, the parent rock plot (C-11) had a dwarf peak at 10 nm (Fig. 5g) and was dominated by a unimodal peak for micro-transition pores (85%). The fractured shale had a bimodal plot with the dominant peaks at approximately 10–20 nm (Fig. 5g), where the highest peak value was < 0.025 mL/g. The samples obtained from the saprock zone had multimodal plots (Fig. 5h) that indicated the samples were dominated by macropores (48–65%). The tallest peak was observed at 3–6 μm with a value of ~0.17 mL/g, where macropores primarily fall in the 2–20 μm range. The transition-pore peak position shifted from 10 nm in the fractured material to 30–50 nm in the saprock zone with peak values up to 1.2–3-fold higher than in fractured sample C-10. In the regolith zone (Fig. 5i), the tallest peaks were at 10–20 μm and formed multimodal plots. Macropores (4–30 μm) were the major contributors to pore volume, making up 68–71% of the pores. Compared with materials obtained from the saprock zone, the volume of 1–2 μm pores in the regolith zone increased and the tallest peak shifted towards larger pore sizes (termed “right shift”).

4.4. Characterization of pore structure

The presence of complex pores in shales from different zones was confirmed by SEM. As shown in Fig. 6, samples contained a large volume of channel and vuggy pores as weathering proceeded. The most common meso-macropore shapes were cylindrical, wedged, triangular, flat, and slit-like (Fig. 6a–b). The dissolved pores formed elliptical or irregularly shaped structures due to mineral dissolution and re-precipitation, including in quartz, plagioclase, carbonate, and pyrite (Figs. 6b–c). Clay minerals commonly occurred as flat particles and resulted in slit-shaped pores (Fig. 6d). In addition, some bottleneck (‘ink bottle’) meso-macropores were identified from the HPMI curve.

Gas isotherm shapes allowed pore shapes to be distinguished by < 100 nm (micro-transition pores in this study) (Rouquerol et al., 1994; Tang et al., 2015). The N_2 adsorption and desorption isotherms for black shale from the three profiles are shown in Fig. 7. According to the International Union of Pure and Applied Chemistry classification (Thommes et al., 2015), the isotherm shapes for all samples were Type IV(a). These shapes could be further divided into hysteresis loop shapes

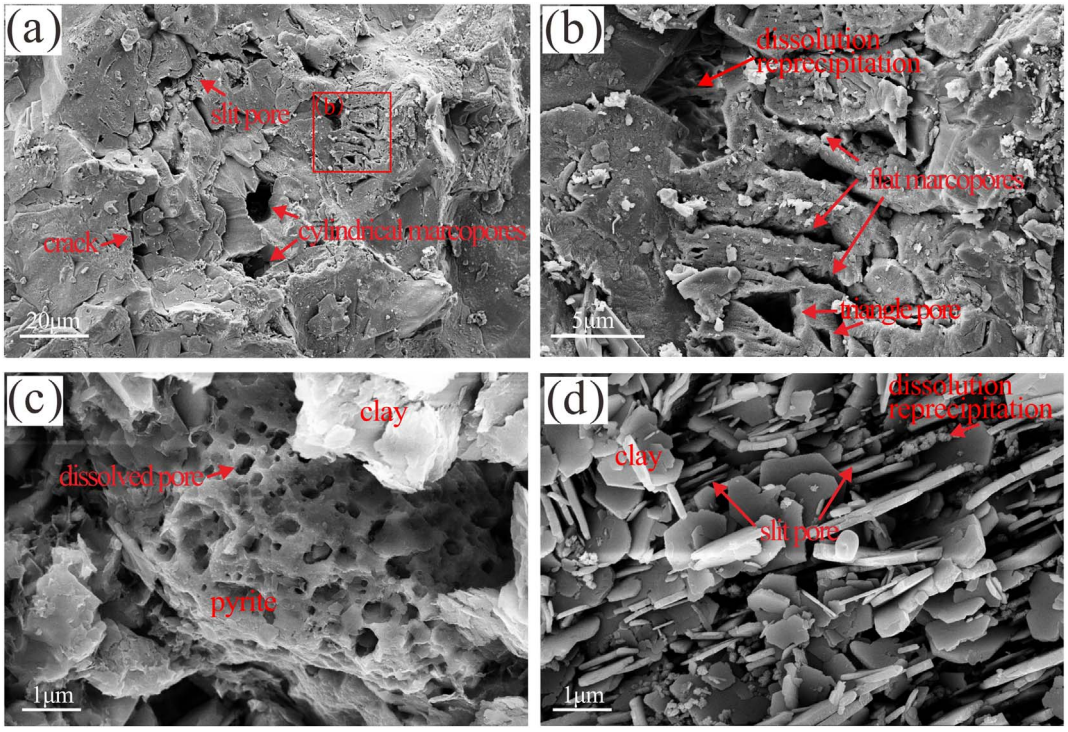

Fig. 6. Pore morphology of SEM images in representative samples. (a–b) cracks, dissolved pores, and intergranular pore from saprock sample (C-5); (c) dissolved pore in pyrite from regolith sample (A-3); (d) slit pore among flat clay mineral particles from regolith sample (C-2).

belonging to Types H4 and H3. Parent and fractured shales contained Type H4 (Figs. 7a–c) hysteresis loops with narrow and slit-like micro-transition pores, suggesting stratification or lamellation pores in the shale. The saprock and regolith samples (Figs. 7d–i) contained Type H3 hysteresis loops, where pores were flat as well as slit-like (Rouquerol et al., 1994; Thommes et al., 2015).

4.5. Fractal dimensions

The fractal dimensions of the pores were calculated using Eqs. (3)–(4) and are summarized in Table 4. Plots of ln(V) vs. $\ln(P_0/P)$ and ln (W_vR^{-2}) vs. $\ln(V^{1/3}R^{-1})$ for representative samples are shown in Appendix Figs. 1–2. After linear fitting, some mesopore fractal dimensions (D_{m1}) were > 3 (Table 4), which did not meet the fractal characteristics under natural conditions (Pfeifer and Avnir, 1983; Fu et al., 2017). These anomalous values (D_{m1} > 3) can also be interpreted as mesopore evolution occurring during weathering.

In profile A, the D_n of micro-transition pores ranged from 2.56 to 2.90. The maximum value of 2.90 was preserved in the parent shale (A-11). The D_n decreased to 2.56 from the parent shale to the upper parts of the saprock zone, but then increased to 2.64 in the regolith zone. Mesopore D_{m1} ranged from 2.62 to 3.51 in profile A, where values were ~3 in both saprock and fractured shales. In addition, D_{m2} ranged from 2.34 towards the parent rock to 2.83 at the surface.

In profile B, D_n ranged from 2.63 to 2.86 with the maximum value found in the parent shale (B-11). Meanwhile, the D_n decreased moving from the parent shale to the surface. D_{m1} ranged from 2.54 to 3.36, where the D_{m1} of the fractured shale was > 3. The lowest D_{m1} value of 2.54 was found in the upper saprock zone at a depth of 2.50 m. D_{m2} ranged from 2.75 to 2.91, where the D_{m2} of parent shale was less than that of other weathered shales.

In profile C, the D_n of micro-transition pores ranged from 2.61 to 2.90 and decreased moving from the parent shale to the surface. D_{m1} ranged from 2.55 to 3.50 and displayed irregular variation along the transect. Conversely, D_{m2} was higher in the weathered shale than in the parent shale with the lowest value being 2.71. D_{m2} increased from 2.71 towards the parent rock to 2.88 at the top of the shale zone (8.00 m). D_{m2} then decreased to 2.81 at depths shallower than 8.00 m in the regolith zone.

5. Discussion

5.1. Evolution of the pore system associated with mineral dissolution/formation

In the regolith and saprock columns, most liquid containing dissolved CO_2 and O_2 advected relatively easily into macropores, but some liquid diffused into micro-transition pores along the entire transect (Bazilevskaya et al., 2013). Liquid also advected through the bedding plane (high-angle dips) and cracks in the saprock and fractured shale zones along weathering profiles (Fig. 1d). These liquids are acidic due to O_2-oxidized pyrite that has diffused to the pore surfaces. Rocks consume H^+ from acidic liquids to different extents depending on their chemical composition and physical properties (e.g., porosity and S_{BET}) (Bazilevskaya et al., 2015; Ling et al., 2016).

Pore diameter increased as the degree of weathering (*CIA*) increased from profiles A to C (Fig. 5), which accelerated liquid-rock interactions during weathering. Micro-transition pores play a key role in O_2 diffusion during weathering, which results in pyrite oxidation and subsequent carbonate dissolution. This phenomenon was consistent with changes in D_n, indicating that micro-transition pores at the surface became smoother during weathering. Meso-macropores play an important role in water-rock interactions, such as carbonate and plagioclase dissolution. Porosity drastically changed in the middle and bottom of the saprock zone and top of the fractured shale in profiles A, B, and C, respectively (Table 1). This change in porosity was accompanied by large variability in bulk density at these depths. Ling et al. (2016) suggested that carbonate and plagioclase dissolution at these depths creates new fractures or meso-macropores and, thus, leads to a dramatic increase in meso-macropores. Carbonate and plagioclase dissolution are the major reactions involved in porosity changes and increase the pore volume during conversion of fractured shale to saprock. However,

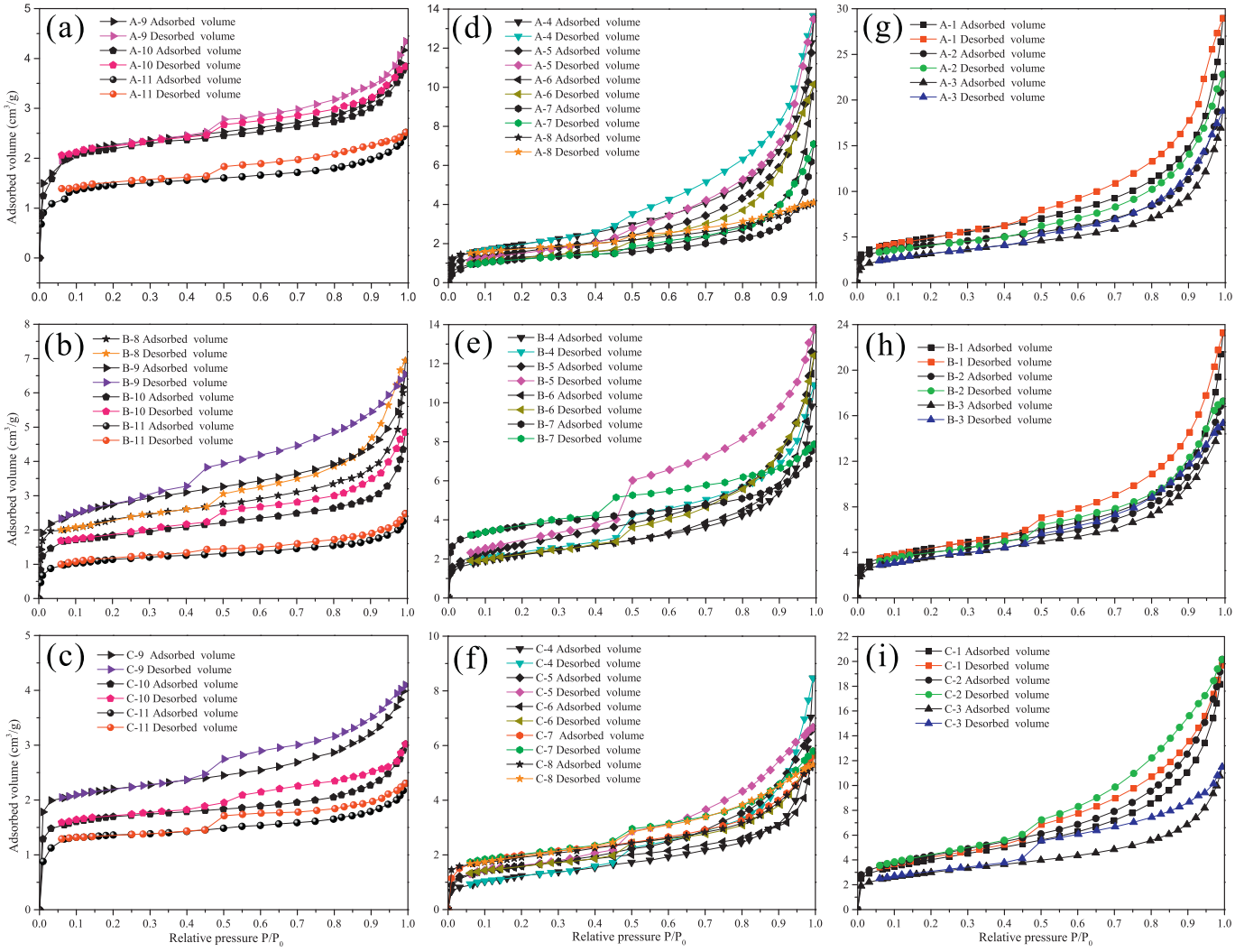

Fig. 7. Low-pressure N_2 adsorption and desorption isotherms of black shales in three profiles. Profile A in (a), (d), and (g); Profile B in (b), (e), and (h); Profile C in (c), (f), and (i). (a–c) parent and fractured shales; (d–f) saprock materials; (g–i) regolith materials.

sulfate (e.g., gypsum), Fe-(oxy)hydroxide, and secondary clay minerals (e.g., kaolinite, smectite, and vermiculite) generally form and re-precipitate on meso-macropore surfaces in saprock and regolith zones (Ling et al., 2016), resulting in roughening of meso-macropores and thereby blocking some connected pores. The D_{m2} increased with decreasing depth, which may be correlated with this reprecipitation and lead to more complex and rougher macropores during weathering. This reprecipitation also contributed to increases in S_{BET} and decreases in bulk density (Table 1).

5.2. Behavior of and relationship between pore fractal dimension and minerals

Pearson correlation coefficients for the relationships between fractal dimensions and mineral content are presented in Table 5. At weak weathering stages (profile A), pyrite and carbonate mineral content were strongly and positively correlated with D_n (A: $r_{Dn\text{-}py} = 0.98$, $r_{Dn\text{-}carb} = 0.90$), but negatively correlated with D_{m2} (A: $r_{Dm2\text{-}py} = -0.91$, $r_{Dm2\text{-}carb} = -0.94$). This phenomenon indicates that pyrite and carbonate dissolution resulted in smoother micro-transition pore surfaces, but rougher and more complex macropore surfaces during weathering. D_{m1} was moderately related to other parameters ($r < 0.43$), indicating that mesopore evolution in profile A was affected by many factors.

At weak-to-moderate weathering stages (profile B), D_n was strongly and positively correlated with pyrite, carbonate, and plagioclase content (B: $r_{Dn\text{-}py} = 0.85$, $r_{Dn\text{-}carb} = 0.84$, $r_{Dn\text{-}plag} = 0.78$). These strong relationships indicate that micro-transition pores were dissolved by acidic liquid through diffusion, thus resulting in smoother pore surfaces. D_{m1} had a strong and positive relationship with plagioclase (B: $r_{Dm1\text{-}plag} = 0.88$), indicating that plagioclase dissolution predominantly occurred in mesopores. D_{m2} had a negative relationship with pyrite and carbonate content (B: $r_{Dm2\text{-}py} = -0.57$, $r_{Dm2\text{-}carb} = -0.41$), suggesting that pyrite and carbonate dissolution led to rougher and more complex macropore surface structures. D_{m2} had a moderate positive correlation with secondary clay minerals (B: $r_{Dm2\text{-}clay} = 0.55$), which could result in more complex macropore structures.

At the moderate-to-intense weathering stage (profile C), D_n had a positive relationship with pyrite, carbonate, and quartz (C: $r_{Dn\text{-}py} = 0.83$, $r_{Dn\text{-}carb} = 0.81$, $r_{Dn\text{-}qua} = 0.80$), suggesting that dissolution of these minerals could lead to smoother micro-transition pore surfaces. Mesopores (D_{m1}) were significantly affected by carbonate dissolution (C: $r_{Dm1\text{-}carb} = 0.86$) and clay mineral formation (C: $r_{Dm1\text{-}clay} = -0.82$), which resulted in smoother mesopore surfaces. Macropore surfaces became more complex with carbonate dissolution (C: $r_{Dm2\text{-}carb} = -0.74$) and clay mineral formation (C: $r_{Dm2\text{-}clay} = 0.63$).

In summary, D_n was strongly and positively correlated with pyrite and carbonate content at the weak-to-intense weathering stages in profiles A to C ($r_{Dn\text{-}py} = 0.98, 0.85, 0.83$; $r_{Dn\text{-}carb} = 0.90, 0.84, 0.81$),

Table 4
Fractal dimensions of pores in black shales derived from HPMI and LP-N_2GA data.

Sample	Depth (m)	Micro-transition pores[a]		Mesopores[b]		Macropores[b]	
		D_n	± [c]	D_{m1}	± [c]	D_{m2}	± [c]
A-1	0.10	2.63	0.02	2.73	0.01	2.83	0.01
A-2	0.25	2.64	< 0.01	2.62	0.01	2.83	0.01
A-3	0.45	2.62	0.02	2.79	0.01	2.86	0.01
A-4	0.55	2.59	0.01	2.79	0.03	2.81	0.01
A-5	0.65	2.56	0.01	3.21	0.04	2.83	0.01
A-6	0.75	2.58	< 0.01	2.99	0.02	2.81	0.01
A-7	0.85	2.66	< 0.01	3.28	0.05	2.80	0.01
A-8	1.10	2.75	0.01	2.99	0.05	2.71	0.01
A-9	1.50	2.88	< 0.01	2.93	0.02	2.64	0.02
A-10	2.10	2.88	< 0.01	3.51	0.05	2.44	0.03
A-11	3.00	2.90	< 0.01	2.75	0.13	2.34	0.03
B-1	0.50	2.64	< 0.01	2.61	0.01	2.87	0.02
B-2	1.00	2.65	< 0.01	2.61	0.01	2.78	0.03
B-3	1.50	2.63	0.01	2.55	0.02	2.83	0.02
B-4	2.00	2.67	0.01	2.57	0.03	2.80	0.03
B-5	2.50	2.63	0.01	2.54	0.03	2.91	0.01
B-6	3.20	2.65	< 0.01	2.76	0.03	2.80	0.01
B-7	4.00	2.83	< 0.01	2.68	0.04	2.86	0.01
B-8	4.80	2.81	< 0.01	3.07	0.06	2.76	0.01
B-9	5.50	2.82	0.02	3.36	0.05	2.82	0.02
B-10	6.20	2.83	< 0.01	3.20	0.12	2.83	0.01
B-11	7.00	2.86	0.01	2.70	0.03	2.75	0.02
C-1	0.50	2.63	< 0.01	2.64	0.01	2.82	0.10
C-2	1.00	2.61	0.01	2.71	0.02	2.82	0.02
C-3	1.50	2.69	< 0.01	2.55	0.01	2.81	0.01
C-4	2.00	2.64	0.01	2.64	0.03	2.84	0.01
C-5	3.00	2.62	0.02	2.73	0.01	2.83	0.01
C-6	4.00	2.74	0.02	2.57	0.01	2.82	0.01
C-7	5.00	2.75	0.02	2.60	0.01	2.85	0.01
C-8	6.20	2.74	< 0.01	2.86	0.01	2.82	0.01
C-9	8.00	2.86	< 0.01	2.68	0.01	2.88	0.01
C-10	9.00	2.89	< 0.01	3.45	0.10	2.72	0.01
C-11	10.50	2.90	< 0.01	3.50	0.08	2.71	0.02

Sample weathering zone is the same as in Table 3 and the fitting correlation coefficients (R^2) are all > 0.95.

[a] The fractal dimension (D_n) from LP-N_2GA using Eq. (4).

[b] The fractal dimension (D_m) from HPMI using Eq. (3).

[c] ± represents the standard errors of D_n, D_{m1}, and D_{m2}, respectively, which are from the standard error of slope in fitting curve.

suggesting that micro-transition pore surfaces became smoother with pyrite and carbonate dissolution as weathering proceeded. D_{m2} was negatively correlated with pyrite and carbonate mineral content, suggesting that pyrite and carbonate dissolution resulted in rougher macropore surfaces. The coefficient between D_{m2} and secondary clay minerals increased from 0.37 to 0.63 as weathering increased, suggesting that clay mineral formation increased the roughness and complexity of macropore surfaces.

5.3. Evolution of clay minerals from weathering

Phyllosilicates from the clay fractions of the saprock and regolith weathering zones were divided into two groups: (1) minerals inherited from parent rocks (illite and muscovite) and (2) secondary minerals (smectite, mixed-layer phases, vermiculite, and kaolinite) (Skiba, 2007; Uzarowicz et al., 2011, 2012). The inheritance of clay fraction constituents from parent rocks was likely from disintegration of large clay particles and dissolution of silicates (Skiba, 2007). Clemente and Azevedo (2007) reported that secondary clay minerals derived from silicates tend to have a 2:1 structure (e.g., illite) when forming near filled cracks and a 1:1 structure (e.g., kaolinite) when forming near well-drained pores.

Secondary clay minerals were observed in the regolith and saprock zones (Figs. 2–5) and were transformed from mica/illite originating in the parent rock or generated from other silicates. At the weak weathering stage (profile A), small amounts of smectite were present in the regolith and top portions of the saprock zones. The M-S/I-S mixed-layer minerals and kaolinite were also present in the regolith zone (Table 2, Fig. 2). Mica (muscovite) transformation into smectite is a typical occurrence in acidic environments (Righi and Meunier, 1991; De Kimpe and Miles, 1992; Uzarowicz et al., 2011, 2012), as in the saprock and regolith zones in profile A, which experienced low pH conditions (lowest pH = 2.68 at 0.65 m). Uzarowicz et al. (2011) reported that mica can directly transform into smectite in a strongly acidic weathering environment. Meanwhile, the M-S/I-S mixed-layer generally acts as a transitional phase during weathering (April et al., 2004; Hazen et al., 2013). Therefore, mica and illite were likely directly transformed into smectite or indirectly transformed with M-S/I-S as an intermediate. Ling et al. (2016) reported that kaolinite is not only derived from plagioclase dissolution, but also phyllosilicate transformation. Based on previous studies (Jackson, 1962; Wilson, 1999; Uzarowicz et al., 2011, 2012; Hazen et al., 2013; Ling et al., 2016), the clay mineral weathering pathway in profile A followed the timeline: Mica/Illite → M-S/I-S mixed-layer → Smectite → Kaolinite.

At the weak-to-moderate weathering stage (profile B), smectite and the M-S/I-S mixed-layer were present in the regolith and saprock zones, the M-V or I-V mixed-layer appeared in the regolith zone, and kaolinite occurred in the regolith and upper parts of the saprock zone (Table 2, Fig. 3). HIV and chlorite was identifiable in the regolith zone. Here, we used the 'chlorite' is assumed to be composed of chlorite, vermiculite and HIV, as described in the next section. The M-V/I-V mixed-layer also acted as a transitional phase as weathering proceeded. Therefore, the clay mineral weathering pathway in profile B may follow the timeline (Jackson, 1962; Churchman, 1980; Churchman and Lowe, 2012; Righi and Meunier, 1991; Uzarowicz et al., 2011, 2012): Mica/Illite → M-S/I-S or M-V/I-S mixed-layer → 'chlorite' (HIV and Ch?) → Smectite → Kaolinite.

At the moderate-to-intense weathering stage (profile C), smectite, kaolinite, and M-V/I-V mixed-layer were present in the regolith and top of the saprock zones, while the M-S/I-S mixed-layer occurred in the

Table 5
Pearson correlation coefficients between fractal dimensions and mineral contents in three weathering profiles. Values > 0.60 are indicated in bold.

	Profile A			Profile B			Profile C		
	D_n	D_{m1}	D_{m2}	D_n	D_{m1}	D_{m2}	D_n	D_{m1}	D_{m2}
Py	**0.98****	0.32	**−0.91****	**0.85****	**0.65***	−0.57	**0.83****	**0.65***	−0.41
Carb	**0.90****	0.27	**−0.94****	**0.84****	0.38	−0.41	**0.81****	**0.86***	**−0.74****
Plag	−0.58	0.02	0.28	**0.78****	**0.88****	−0.36	−0.22	0.27	−0.44
Qua	**−0.66***	−0.07	0.43	−0.56	**−0.71***	0.04	**0.80****	0.58	−0.39
Clay	−0.14	−0.44	0.37	−0.41	−0.37	0.55	**−0.93****	**−0.82****	**0.63***

Py: pyrite, Carb: carbonate (calcite + dolomite), Plag: plagioclase, Clay: secondary clay minerals, Qua: quartz. The mineral contents are quoted from Ling et al. (2016).

** $p < 0.01$.

* $p < 0.05$.

regolith and saprock zones (Table 2, Fig. 4). Vermiculite, one of products of mica/illite transformation in the weathering zone, appeared in the regolith and upper parts of the saprock zones. The presence of vermiculite minerals indicates that transformation proceeded through an intermediate M-V/I-V mixed-layer (Bain et al., 1990; Wilson, 1999; Hong et al., 2014). HIV was clearly identifiable in the regolith zone. These hydroxy-interlayers were likely formed by the deposition of Al-hydroxy polymers in the vermiculite interlayer space (Wilson, 1999). Mica and illite have been shown to form HIV and kaolinite under acidic weathering conditions (Buol and Weed, 1991). Small amounts of the K-S mixed-layer were observed in surface sample C-1 (Fig. 4) and probably formed as an intermediate of the smectite to kaolinite transition (Delvaux and Herbillon, 1995; Dudek et al., 2007; Hong et al., 2012). The final weathering product gibbsite, i.e., only Al- (hydr-) oxide, was also observed in the top of the regolith zone. The sequence of changes to clay species in profile C going from deeper to shallower likely followed the timeline (Churchman, 1980; Churchman and Lowe, 2012; Bain et al., 1990; Wilson, 1999; Skiba, 2007; Uzarowicz et al., 2011, 2012; Hong et al., 2012, 2014):

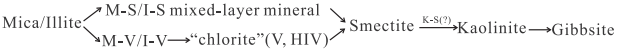

In addition, the depth of secondary clay mineral formation deepened with increasing *CIA* in profiles A to C (Table 2). These secondary clay minerals not only formed from silicate dissolution, but also from both primary and secondary clay mineral dissolution and transformation in the acidic environment present during black shale weathering. Clay mineral dissolution likely occurs simultaneously with the transformation of clay minerals into secondary minerals. In this study, we used the 'chlorite' represented as vermiculite, HIV, and chlorite pedogenic process that occurs in black shale weathering systems. The sequence of the clay minerals that appear under acidic conditions in black shale from weathering in this region can be summarized as follows:

(1) Mica (muscovite) → M-S or M-V → 'chlorite' (V, HIV?, and Ch?) → Smectite → Kaolinite → Gibbsite
(2) Illite → I-S or I-V → 'chlorite' (V?) → Smectite → Kaolinite → Gibbsite

6. Conclusion

Based on the results of this present study, the following can be concluded:

(1) Pore diameter increased moving from the parent shale to the surface, as well as with increasing degrees of weathering. This results in decreases in density and increases in porosity and S_{BET} during weathering. The micro-transition pores changed from narrow, slit-like pores in the parent shale to flat, slit-shaped pores in weathered samples accompanied by the formation of clay mineral. However, the different mesopore and macropore shapes were preserved during weathering.
(2) Fractal dimensions D_n, D_{m1}, and D_{m2} can be used to characterize the structures of micro-transition pores, mesopores, and macropores, respectively. Pyrite oxidation and carbonate dissolution led to smoother micro-transition pore surfaces in a manner positively correlated with D_n. However, D_{m2} was negatively correlated with pyrite and carbonate content and weathering resulted in rougher and more complex macropore surfaces. The influence of clay mineral formation on fractal dimensions increased with increasing degrees of weathering. Clay mineral formation increased the smooth micro-transition and mesopore surfaces as well as the rougher and more complex macropore surfaces observed during weathering.
(3) Inheritance of the phyllosilicates mica and illite from parent shales was notable in the acidic weathering systems present in pyrite-bearing black shale. Clay minerals formed from silicate (e.g., plagioclase) dissolution, disintegration of larger grains of micas and illite, and transformation of transitional clay minerals, including interlayer minerals. The depth of secondary clay mineral formation deepened with increased weathering. This silicate dissolution and clay mineral transformation likely occurred simultaneously with weathering.
(4) The potential sequence of clay mineral in black shale weathering systems is as follows: M/I → M-S/I-S or M-V/I-V mixed-layer → 'chlorite' (V, HIV?, and Ch?) → S → K → G. Weathering product formation, including transitional phases, correlated with weathering intensity, weathering zones, and geomorphological position. In addition, mica/illite can directly transform into smectite without proceeding through other intermediate phases.

Acknowledgments

The present work was supported by research funds awarded by the National Natural Science Foundation of China (No. 41472256, 41502269), and Fundamental Research Funds for the Central Universities (No. 2682017CX078). The authors thank the official editors and three anonymous reviewers for their critical comments and valuable suggestions.

Appendix A. Supplementary data

Supplementary data to this article can be found online at https://doi.org/10.1016/j.gexplo.2018.02.002.

References

Ahmad, A.L., Mustafa, N.N.N., 2006. Pore surface fractal analysis of palladium-alumina ceramic membrane using Frenkel-Halsey-Hill (FHH) model. J. Colloid Interface Sci. 31, 575–584. http://dx.doi.org/10.1016/j.jcis. 2006.05.041.
April, R.H., Keller, D., Driscoll, T., 2004. Smectite in spodosols from the Adirondack Mountains of New York. Clay Miner. 39, 99–113. http://dx.doi.org/10.1180/0009855043910123.
Avnir, D., Farin, D., 1983. Chemistry in noninteger dimensions between two and three. II. Fractal surfaces of adsorbents. J. Chem. Phys. 79 (7), 33566–33571. http://dx.doi.org/10.1063/1.446211.
Bain, D.C., Mellor, A., Wilson, M.J., 1990. Nature and origin of an aluminous vermiculitic weathering product in acid soils from upland catchments in Scotland. Clay Miner. 25, 467–475. http://dx.doi.org/10.1180/claymin.1990.025.4.05.
Bazilevskaya, E., Lebedeva, M., Pavich, M., Rother, G., Parkinson, D.Y., Cole, D., Brantley, S.L., 2013. Where fast weathering creates thin regolith and slow weathering creates thick regolith. Earth Surf. Process. Landf. 38, 847–858. http://dx.doi.org/10.1002/esp.3369.
Bazilevskaya, E., Rother, G., Mildneer, D.F.R., Pavich, M., Cole, D., Bhatt, M.P., Jin, L., Steefel, C.I., Brantley, S.L., 2015. How oxidation and dissolution in diabase and granite control porosity during weathering. Soil Sci. Soc. Am. J. 79, 55–73. http://dx.doi.org/10.2136/sssaj.2014.04.0135.
Behrens, R., Bouchez, J., Schuessler, J.A., 2015. Mineralogical transformations set slow weathering rates in low-porosity metamorphic bedrock on mountain slopes in a tropical climate. Chem. Geol. 411, 283–298. http://dx.doi.org/10.1016/j.chemgeo.2015.07.008.
Borrelli, L., Perri, F., Critelli, S., Gullà, G., 2014. Characterization of granitoid and gneissic weathering profiles of the Mucone basin (Calabria, southern Italy). Catena 113, 325–340. http://dx.doi.org/10.1016/j.catena.2013.08.014.
Brunauer, S., Emmett, P.H., Teller, E., 1938. Adsorption of gases in multimolecular layers. J. Am. Chem. Soc. 60, 309–319. http://dx.doi.org/10.1021/ja01269a023.
Buol, S.W., Weed, S.B., 1991. Saprolite-soil transformations in the Piedmont and mountains of North Carolina. Geoderma 51, 15–28. http://dx.doi.org/10.1016/0016-7061(91)90064-Z.
Cai, Y., Liu, D., Pan, Z., Yao, Y., Li, J., Qiu, Y., 2013. Pore structure and its impact on CH_4 adsorption capacity and flow capability of bituminous and subbituminous coals from Northeast China. Fuel 103, 258–268. http://dx.doi.org/10.1016/j.fuel.2012.06.055.
Chigira, M., Nakamoto, M., Nakata, E., 2002. Weathering mechanisms and their effects on the landsliding of ignimbrite subject to vapor-phase crystallization in the Shirakawa pyroclastic flow, northern Japan. Eng. Geol. 66, 111–125. http://dx.doi.org/10.1016/S0013-7952(02)00035-2.
Churchman, C.J., 1980. Clay minerals formed from micas and chlorites in some New Zealand soils. Clay Miner. 15, 59–76. http://dx.doi.org/10.1180/claymin.1980.015.1.05.
Churchman, G.J., Lowe, D.J., 2012. Alteration, formation and occurrence of minerals in soils. In: Huang, P.M., Li, Y., Sumner, M.E. (Eds.), Handbook of Soil Science, 2nd Edition, Properties and Processes. CRC Press (Taylor & Francis), Boca Raton, Florida,

pp. 20.1–20.72.
Clemente, C.A., Azevedo, A.C., 2007. Mineral weathering in acid saprolites from subtropical, Southern Brazil. Sci. Agric. 64, 601–607. http://dx.doi.org/10.1590/S0103-90162007000600007.
Cousin, I., Nicoullaud, B., Coutadeur, C., 2003. Influence of rock fragments on the water retention and water percolation in a calcareous soil. Catena 53, 97–114. http://dx.doi.org/10.1016/S0341-8162(03) 00037-7.
De Kimpe, C., Miles, N., 1992. Formation of swelling clay minerals by sulfide oxidation in some metamorphic rocks and related soils of Ontario, Canada. Can. J. Soil Sci. 72, 263–270. http://dx.doi.org/10.4141/cjss92-025.
Delvaux, B., Herbillon, A.J., 1995. Pathways of mixed layer kaolin-smectite formation in soils. In: Proceedings 10th International Clay Conference, Adelaide, pp. 457–461.
Dudek, T., Cuadros, J., Huertas, J., 2007. Structure of mixed-layer kaolinite-smectite and smectite to kaolinite transformation mechanism from synthesis experiments. Am. Mineral. 92, 179–192. http://dx.doi.org/10.2138/am.2007.2218.
Egli, M., Merkli, C., Sartori, G., Mirabella, A., Plötze, M., 2008a. Weathering, mineralogical evolution and soil organic matter along a Holocene soil toposequence developed on carbonate-rich materials. Geomorphology 97, 675–696. http://dx.doi.org/10.1016/j.geomorph.2007.09. 011.
Egli, M., Mirabella, A., Sartori, G., 2008b. The role of climate and vegetation in weathering and clay mineral formation in late Quaternary soils of the Swiss and Italian Alps. Geomorphology 201, 307–324. http://dx.doi.org/10.1016/j.geomorph.2008.04.001.
Fischer, C., Gaupp, R., 2005. Change of black shale organic material surface area during oxidative weathering: implications for rock-water surface evolution. Geochim. Cosmochim. Acta 69, 1213–1224. http://dx.doi.org/10.1016/j.gca.2004.09.021.
Fischer, C., Schmidt, C., Bauer, A., Gaupp, R., Heide, K., 2009. Mineralogical and geochemical alteration of low-grade metamorphic black slates due to oxidative weathering. Chem. Erde 69, 127–142. http://dx.doi.org/10.1016/j.chemer.2009.02.002.
Fletcher, R.C., Buss, H.L., Brantley, S.L., 2006. A spheroidal weathering model coupling porewater chemistry to soil thickness during steady-state denudation. Earth Planet. Sci. Lett. 244, 444–457. http://dx.doi.org/10.1016/j.epsl.2006. 01.055.
Fu, H., Tang, D., Xu, T., Xu, H., Tao, S., Li, S., Yin, Z.Y., Chen, B., Zhang, C., Wang, L., 2017. Characteristics of pore structure and fractal dimension of low-rank coal: a case study of Lower Jurassic Xishanyao coal in the southern Junggar Basin, NW China. Fuel 193, 254–264. http://dx.doi.org/10.1016/j.fuel.2016.11.069.
GB/T 50266-2013, 2013. Standard for Test Methods of Engineering Rock Mass. China Planning Press, Beijing (in Chinese).
Harris, W.G., Morrone, A.A., Coleman, S.E., 1992. Occluded mica in hydroxy-interlayered vermiculite grains from a highly-weathered soil. Clay Clay Miner. 40, 32–39. http://dx.doi.org/10.1346/CCMN.1992.0400105.
Hazen, R.M., Sverjensky, D.A., Azzoliini, D., Bish, D.L., Elmore, S.C., Hinnov, L., Milliken, R.E., 2013. Clay mineral evolution. Am. Mineral. 98, 2007–2029. http://dx.doi.org/10.2138/am.2013.4425.
Hodot, B.B., 1966. In: Song, S.Z., Wang, Y.A. (Eds.), Outburst of Coal and Coalbed Gas (Chinese Translation). China Industry Press, Beijing, pp. 23–25.
Hong, H., Churchman, G.J., Gu, Y., Wang, C., 2012. Kaolinite-smectite mixed-layer clays in the Jiujiang red soils and their climate significance. Geoderma 173–174, 75–83. http://dx.doi.org/10.1016/j.geoderma.2011.12.006.
Hong, H., Churchman, G.J., Yin, K., Li, R., Li, Z., 2014. Randomly interstratified illite-vermiculite from weathering of illite in red earth sediments in Xuancheng, southeastern China. Geoderma 214–215, 42–49. http://dx.doi.org/10.1016/j.geoderma.2013. 10.004.
Hu, J., Tang, S., Zhang, S., 2016. Investigation of pore structure and fractal characteristics of the Lower Silurian Longmaxi shales in western Hunan and Hubei provinces in China. Journal of Natural Gas Science and Engineering 28, 522–535. http://dx.doi.org/10.1016/j.jngse.2015.12.024.
Jackson, M.L., 1962. Interlayering of expansible layer silicates in soils by chemical weathering. Clay Clay Miner. 11, 29–46. http://dx.doi.org/10.1346/CCMN.1962.0110104.
Jackson, M.L., 1978. Soil Chemistry Analysis. University of Wisconsin, Madison, USA (Self-Published).
Jaffe, L.A., Peucker-Ehrenbrink, B., Petsch, S.T., 2002. Mobility of rhenium, platinum group elements and organic carbon during black shale weathering. Earth Planet. Sci. Lett. 198, 339–353. http://dx.doi.org/10.1016/S0012-821X(02)00526-5.
Jamtveit, B., Kobchenko, M., Austrheim, H., Malthe-Sørenssen, A., Røyne, A., Svensen, H., 2011. Porosity evolution and crystallization-driven fragmentation during weathering of andesite. J. Geophys. Res. 116, B12204. http://dx.doi.org/10.1029/2011JB00008649.
Jin, L., Ravella, R., Ketchum, B., Bierman, P.R., Heaney, P., White, T., Brantley, S.L., 2010. Mineral weathering and elemental transport during hillslope evolution at the Susquehanna/Shale Hills Critical Zone Observatory. Geochim. Cosmochim. Acta 74, 3669–3691. http://dx.doi.org/10.1016/j.gca.2010.03.036.
Jin, L., Rother, G., Cole, D.R., Mildner, D.F.R., 2011. Characterization of deep weathering and nanoporosity development in shale—a neutron study. Am. Mineral. 96, 498–512. http://dx.doi.org/10.2138/am.2011.3598.
Jin, L., Mathur, R., Rother, G., Cole, D., Bazilevskaya, E., Williams, J., Carone, A., Brantley, S., 2013. Evolution of porosity and geochemistry in Marcellus Formation black shale during weathering. Chem. Geol. 356, 50–63. http://dx.doi.org/10.1016/j.chemgeo.2013.07.012.
Kuila, U., Prasad, M., 2011. Understanding Pore-structure and Permeability in Shales: SPE Annual Technical Conference and Exhibition, Denver, Colorado, 2011, SPE Paper 146869. http://dx.doi.org/10.2118/146869-MS. (13 pp.).
Langman, J.B., Blowes, D.W., Sinclair, S.A., Krenta, A., Amos, R.T., Smith, L.J.D., Pham, H.N., Sego, D.C., Smith, L., 2015. Early evolution of weathering and sulfide depletion of a low-sulfur, granitic, waste rock in an Arctic climate: a laboratory and field site comparison. J. Geochem. Explor. 156, 61–71. http://dx.doi.org/10.1016/j.gexplo.2015.05. 004.
Liao, X., Chigira, M., Matsushi, Y., Wu, X.Y., 2014. Investigation of water-rock interactions in Cambrian black shale via a flow-through experiment. Appl. Geochem. 51, 65–78. http://dx.doi.org/10.1016/j.apgeochem.2014.09.012.
Ling, S.X., Wu, X.Y., Ren, Y., Sun, C.W., Liao, X., Li, X.N., Zhu, B.L., 2015. Geochemistry of trace and rare earth elements during weathering of black shale profiles in Northeast Chongqing, Southwestern China: their mobilization, redistribution, and fractionation. Chem. Erde 75, 403–417. http://dx.doi.org/10.1016/j.chemer.2015.07.004.
Ling, S.X., Wu, X.Y., Sun, C.W., Liao, X., Ren, Y., Li, X.N., 2016. Mineralogy and geochemistry of three weathered Lower Cambrian black shale profiles in Northeast Chongqing, China. Geosci. J. 20, 793–812. http://dx.doi.org/10.1007/s12303-016-0008-y.
Mahamud, M.M., Novo, M.F., 2008. The use of fractal analysis in the textural characterization of coals. Fuel 87, 222–231. http://dx.doi.org/10.1016/j.fuel.2007.04.020.
Navarre-Sitchler, A., Steefel, C.I., Yang, L., Tomutsa, L., Brantley, S.L., 2009. Evolution of porosity and diffusivity associated with chemical weathering of a basalt clast. J. Geophys. Res. 114, F02016. http://dx.doi.org/10.1029/2008JF001060.
Navarre-Sitchler, A.K., Cole, D.R., Rother, G., Jin, L., Buss, H.L., Brantley, S.L., 2013. Porosity and surface area evolution during weathering of two igneous rocks. Geochim. Cosmochim. Acta 109, 400–413. http://dx.doi.org/10.1016/j.gca.2013.02.012.
Navarre-Sitchler, A., Brantley, S.L., Rother, G., 2015. How porosity increases during incipient weathering of crystalline silicate rocks. Rev. Mineral. Geochem. 80, 331–354. http://dx.doi.org/10.2138/rmg.2015.80.10.
Peng, B., Rate, A., Song, Z.L., Yu, C.X., Tang, X.Y., Xie, S.R., Tu, X.L., Tan, C.Y., 2014. Geochemistry of major and trace elements and Pb-Sr isotopes of a weathering profile developed on the Lower Cambrian black shales in central Hunan, China. Appl. Geochem. 51, 191–203. http://dx.doi.org/10.1016/j.apgeochem. 2014.09.007.
Perri, F., Scarciglia, F., Apollaro, C., Marini, L., 2015. Characterization of granitoid profiles in the Sila Massif (Calabria, southern Italy) and reconstruction of weathering processes by mineralogy, chemistry, and reaction path modeling. J. Soils Sediments 15, 1351–1372. http://dx.doi.org/10.1007/s11368-014-0856-x.
Perri, F., Ietto, F., Le Pera, E., Apollaro, C., 2016. Weathering processes affecting granitoid profiles of Capo Vaticano (Calabria, southern Italy) based on petrographic, mineralogic and reaction path modeling approaches. Geol. J. 51, 368–386. http://dx.doi.org/10.1002/gj.2635.
Pfeifer, P., Avnir, D., 1983. Chemistry in noninteger dimensions between two and three. I. Fractal theory of heterogeneous surfaces. J. Chem. Phys. 79, 3558–3565. http://dx.doi.org/10.1063/1.446210.
Poppe, L.J., Paskevich, V.F., Hathaway, J.C., Blackwood, D.S., 2002. A laboratory manual for X-ray powder diffraction. In: U.S. Geological Survey Open File Report 01-041. U.S. Geological Survey, MA. http://pubs.usgs.gov/openfile/0f01-041/index.htm.
Righi, D., Meunier, A., 1991. Characterization and genetic interpretation of clays in an acid brown soil (Dystrochrept) developed in a granitic saprolite. Clay Clay Miner. 39, 519–530. http://dx.doi.org/10.1346/CCMN.1991.0390507.
Rouquerol, J., Avnir, D., Fairbridege, C.W., Everett, D.H., Haynes, J.M., Pernicone, N., Ramsay, J.D.F., Sing, K.S.W., Unger, K.K., 1994. Recommendations for the characterization of porous solids (technical report). Pure Appl. Chem. 66, 1739–1758. http://dx.doi.org/10.1351/pac199466081739.
Schultz, L.G., Shepard, A.O., Blackmon, P.D., Starkey, H.C., 1971. Mixed-layer kaolinite-montmorillonite from the Yucatan Peninsula, Mexico. Clay Clay Miner. 19, 137–150. http://dx.doi.org/10.1346/CCMN.1971.0190302.
Skiba, M., 2007. Clay mineral formation during podzolization in an alpine environment of the Tatra Mountains, Poland. Clay Clay Miner. 55, 618–634. http://dx.doi.org/10.1346/CCMN.2007.0550609.
Squires, T.M., Quake, S.R., 2005. Microfluidics: fluid physics at the nanoliter scale. Rev. Mod. Phys. 77, 977–1026. http://dx.doi.org/10.1103/RevModPhys.77.977.
Tang, X., Jiang, Z., Li, Z., Gao, Z., Bai, Y., Zhao, S., Feng, J., 2015. The effect of the variation in material composition on the heterogeneous pore structure of high-maturity shale of the Silurian Longmaxi formation in the southeastern Sichuan Basin, China. J. Nat. Gas Sci. Eng. 23, 464–473. http://dx.doi.org/10.1016/j.jngse.2015.02.031.
Thommes, M., Kaneko, K., Neimark, A.V., Olivier, J.P., Rodriguez-Reinoso, F., Rouquerol, J., Sing, K.S.W., 2015. Physisorption of gases, with special reference to the evaluation of surface area and pore size distribution (IUPAC technical report). Pure Appl. Chem. 87, 1051–1069. http://dx.doi.org/10.1515/pac-2014-1117.
Uzarowicz, L., Skiba, S., Skiba, M., Šegvić, B., 2011. Clay-mineral formation in soils developed in the weathering zone of pyrite-bearing schists: a case study from the abandoned pyrite mine in Wieściszowice, Lower Silesia, SW Poland. Clay Clay Miner. 59, 581–594. http://dx.doi.org/10.1346/CCMN.2011.0590604.
Uzarowicz, L., Šegvić, B., Michalik, M., Bylina, P., 2012. The effect of hydrochemical conditions and pH of the environment on phyllosilicate transformations in the weathering zone of pyrite-bearing schists in Wieściszowice (SW Poland). Clay Miner. 47, 401–417. http://dx.doi.org/10.1180/claymin.2012.047.4.01.
Wang, L., Li, Y., Wang, H.R., Cui, X.L., Wang, X., Lu, A.H., Wang, X., Wang, C.Q., Gan, D.Q., 2017. Weathering behavior and metal mobility of tailings under an extremely arid climate at Jinchuan Cu-Ni sulfide deposit, Western China. J. Geochem. Explor. 173, 1–12. http://dx.doi.org/10.1016/j.gexplo.2016.11.009.
Washburn, E.W., 1921. Note on a method of determining the pore-size distribution in porous material. Proc. Natl. Acad. Sci. U. S. A. 7, 115–116. http://dx.doi.org/10.1073/pnas.7.4.115.
Wilson, M.J., 1999. The origin and formation of clay minerals in soils: past, present and future perspectives. Clay Miner. 34, 7–25. http://dx.doi.org/10.1180/

000985599545957.
Wu, X.Y., Ling, S.X., Liao, X., Li, J.W., Zhao, S.Y., Zhang, J.H., 2015. Weathering geochemical behavior and slope failure characteristics of black strata in Guizhou and Guangxi province, Southwest China. In: Engineering Geology for Society and Territory. 2. Springer International Publishing, pp. 1099–1104. http://dx.doi.org/10.1007/978-3-319-09057-3_194.
Yao, Y.B., Liu, D.M., Tang, D.Z., Tang, S.H., Huang, W.H., Liu, Z.H., Che, Y., 2009. Fractal characterization of seepage-pores of coals from China: an investigation on permeability of coals. Comput. Geosci. 35, 1159–1166. http://dx.doi.org/10.1016/j.cageo.2008.09.005.
Zhang, B.Q., Li, S.F., 1995. Determination of the surface fractal dimension for porous media by mercury porosimetry. Ind. Eng. Chem. Res. 34, 1383–1386. http://dx.doi.org/10.1021/ie00043a044.
Zhang, B.Q., Liu, W., Liu, X.F., 2006. Scale-dependent nature of the surface fractal dimension for bi- and multi-disperse porous solids by mercury porosimetry. Appl. Surf. Sci. 253, 1349–1355. http://dx.doi.org/10.1016/j.apsusc.2006.02.009.